ORIGINAL PAPER



Hyper-viscoelastic damage modeling of whole blood clot under large deformation

Manuel K. Rausch² • Gabriella P. Sugerman² • Sotirios Kakaletsis¹ • Berkin Dortdivanlioglu^{3,4}

Received: 2 February 2021 / Accepted: 15 May 2021 / Published online: 2 June 2021 © The Author(s), under exclusive licence to Springer-Verlag GmbH Germany, part of Springer Nature 2021

Abstract

Blood clots play a diametric role in our bodies as they are both vital as a wound sealant, as well as the source for many devastating diseases. In blood clots' physiological and pathological roles, their mechanics play a critical part. These mechanics are non-trivial owing to blood clots' complex nonlinear, viscoelastic behavior. Casting this behavior into mathematical form is a fundamental step toward a better basic scientific understanding of blood clots, as well as toward diagnostic and prognostic computational models. Here, we identify a hyper-viscoelastic damage model that we fit to original data on the nonlinear, viscoelastic behavior of blood clots. Our model combines the classic Ogden hyperelastic constitutive law, a finite viscoelastic model for large deformations, and a non-local, gradient-enhanced damage formulation. By fitting our model to cyclic tensile test data and extension-to-failure data, we inform the model's nine unknown material parameters. We demonstrate the predictability of our model by validating it against unseen cyclic tensile test and stress-relaxation data. Our original data, model formulation, and the identified constitutive parameters of this model are openly available for others to use, which will aid in developing accurate, quantitative simulations of blood clot mechanics.

Keywords Nonlocal damage · Finite viscoelasticity · Thrombus · Finite element

1 Introduction

Blood clots play a diametric role in our bodies. On one hand, blood clots form at the site of vascular injury to prevent hemorrhage (Esmon 2009). On the other hand, blood clots may also form within our vasculature where they can emobolize and occlude blood flow to vital organs causing devastating diseases such as heart attacks, strokes, and pulmonary embolisms (Wendelboe and Raskob 2016). Understanding blood clots' mechanical properties is critical to

understanding both of these roles. For instance, the ability of a clot to undergo very large deformations and resist fracture is important to its role as a wound sealant (Sugerman et al. 2020a). Similarly, blood clots' ability (or inability) to resist hemodynamic forces critically determines whether thrombus embolizes and causes aforementioned deadly diseases (Tutwiler et al. 2020).

Because of the physiological and pathological importance of blood clots, numerous studies have investigated blood clot mechanics, which have been excellently reviewed by others (Johnson et al. 2017). To provide context for this work, we provide a brief overview below. Blood clots are highly hydrated, composite biomaterials comprised of formed elements, red blood cells and platelets, within a fibrin biopolymer network (Cines et al. 2014; Gersh et al. 2009). This composition leads to a highly deformable, soft, initially isotropic material that exhibits a negative Poynting effect, i.e., contraction under shear (Di Martino et al. 1998; Sugerman et al. 2020a). Additionally, the material is viscoelastic such that its mechanics are strain-rate dependent, exhibit hysteresis, Mullin's-like damage, nonlinear stress relaxation, and set (van Kempen et al. 2016; van Dam et al. 2008; Lee et al. 2015; Malone et al. 2018; Sugerman et al. 2020a). In

- Manuel K. Rausch manuel.rausch@utexas.edu
- Department of Aerospace Engineering and Engineering Mechanics, University of Texas at Austin, 2617 Wichita Street, Austin, TX 78712, USA
- Department of Biomedical Engineering, University of Texas at Austin, Austin, TX 78712, USA
- Department of Civil, Architectural and Environmental Engineering, The University of Texas at Austin, Austin, TX 78712, USA
- Oden Institute for Computational Engineering and Sciences, The University of Texas at Austin, Austin, TX 78712, USA



summary, blood clots are mechanically complex materials. Numerous previous efforts have attempted to cast this behavior into constitutive models (Geest et al. 2006; Rausch and Humphrey 2016, 2017; Sugerman et al. 2020a; van Kempen et al. 2016). While many models have successfully captured limited aspects of this complex behavior into mathematical form, none have so far included blood clots' viscoelastic behavior, damage behavior, and large deformation behavior into a single, comprehensive model.

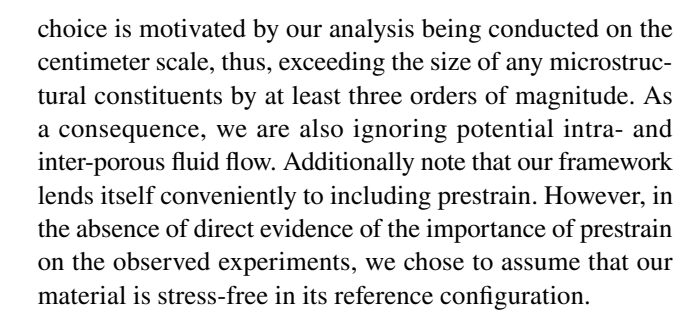
Our failure to develop a comprehensive, quantitatively accurate model of blood clots' mechanics has been a stumbling block to a more fundamental understanding of blood clots' physiology and pathology (Reeps et al. 2013; Sengupta et al. 2014; Khodaee et al. 2016). For instance, understanding blood clots' role in stroke, heart attack, and pulmonary embolism requires quantification of their fracture properties (Gasser et al. 2008; Tutwiler et al. 2020). In turn, this requires detailed fracture studies that enable differentiation between intrinsic toughness from other dissipative mechanisms. To do so in a complex material such as blood clot, it requires detailed, comprehensive models that include viscoelasticity and damage behavior (Zhang et al. 2015).

The objective of this work is to develop and fit a viscoelastic damage model for blood clots under large deformation as step toward establishing a quantitative and predictive model of blood clots' mechanics. To this end, we first combine a hyper-viscoelastic framework with a gradientenhanced damage modeling approach. We then collect a comprehensive set of mechanical data on blood clots' viscoelastic-damage behavior under large deformation. We use a subset of these data to train our model before validating its suitability against left-out test data.

2 Methods

2.1 Non-local damage formulation coupled with finite viscoelasticity

Modeling the structural behavior of large viscoelastic deformations and damage to the material is formulated as a coupled two-field problem, characterized by the deformation field φ and the non-local damage field φ . In this section, we first briefly review the constitutive relations for the finite viscoelasticity model of Reese and Govindjee that considers large deformations and large deviations away from thermodynamic equilibrium (Reese and Govindjee 1998). Then, we subsequently incorporate damage-induced softening of the constitutive behavior through a non-local damage formulation, detailed in Ostwald et al. (2019), Waffenschmidt et al. (2014), Schulte et al. (2020). Please note, in our effort to describe the macromechanics of blood clots, we treat it in subsequent derivations as a single-phase continuum. This



2.1.1 Finite viscoelasticity

Consider a continuum body that occupies the reference configuration \mathcal{B} at time t=0. The nonlinear deformation field φ relates reference positions X to current positions $x = \varphi(X,t)$ at any time t>0, whereas its material gradient defines the deformation gradient F = Grad φ . To account for the inelastic (viscous) effects, a multiplicative decomposition of the deformation into elastic and viscous parts $F = F_e \cdot F_v$ is adopted. Accordingly, the *local* free energy density per unit volume in the material configuration is additively split into two parts 1

$$\Psi = \Psi(\boldsymbol{C}, \boldsymbol{F}_{v}) = \Psi_{EO}(\boldsymbol{C}) + \Psi_{NEO}(\boldsymbol{F}_{v}^{-T} \cdot \boldsymbol{C} \cdot \boldsymbol{F}_{v}^{-1}), \tag{1}$$

where $\Psi_{\rm EQ}$ and $\Psi_{\rm NEQ}$ correspond to purely elastic (equilibrium) and viscous (non-equilibrium) response, respectively. The non-equilibrium part leads to creep and relaxation behavior of the material, and it depends on the elastic counterpart of the right Cauchy–Green tensor $C_e = F_v^{-1} \cdot C \cdot F_v^{-1}$. The second Piola–Kirchhoff stress tensor can be calculated as

$$S = 2\frac{\partial \Psi}{\partial C} = 2\frac{\partial \Psi_{EQ}}{\partial C} + 2[F_v]^{-1} \cdot \frac{\partial \Psi_{NEQ}}{\partial C} \cdot [F_v]^{-T}.$$
 (2)

Assuming an isotropic material response, we can then represent the free energy (1) in terms of principal values (Sugerman et al. 2020a). Similarly, the Kirchhoff stress $\tau = F \cdot S \cdot F^{T}$ reads

$$\tau = \sum_{i=1}^{3} [\tau_{\text{EQ}}]_i \, \boldsymbol{n}_i \otimes \boldsymbol{n}_i + \sum_{i=1}^{3} [\tau_{\text{NEQ}}]_i \, \boldsymbol{n}_i \otimes \boldsymbol{n}_i \tag{3}$$

where n_i are the principal normalized eigenvectors. The eigenvalues $[\tau_{\rm EQ}]_i$ and $[\tau_{\rm NEQ}]_i$ are expressed using the principal stretches λ_i and $[\lambda_e]_i$ of F and its elastic part F_e , respectively,



¹ To account for multiple relaxation mechanisms $(k=1,\ldots,n)$, one can modify the local free energy as $\Psi=\Psi(C,F_{\nu}^1,\ldots,F_{\nu}^n)=\Psi_{\rm EQ}(C)+\sum_{k=1}^n\Psi_{\rm NEQ}^k([F_{\nu}^k]^{-{\rm T}}\cdot C\cdot [F_{\nu}^k]^{-1})$. In the numerical calculations, we adopt n=2 considering both short-term and long-term behaviors of the material.

$$[\tau_{\rm EQ}]_i = \lambda_i \frac{\partial \Psi_{\rm EQ}}{\partial \lambda_i}$$
 and $[\tau_{\rm NEQ}]_i = [\lambda_e]_i \frac{\partial \Psi_{\rm NEQ}}{\partial [\lambda_e]_i}$. (4)

In what follows, we assume an isotropic compressible N=1-Ogden material model for both the equilibrium and the non-equilibrium states (Ogden 1973). For extensions to anisotropic finite strain viscoelasticity suitable for fibrous soft tissues, see (Latorre and Montáns 2015; Liu et al. 2019). For the sake of brevity, we report the derivations only for the non-equilibrium part. For more details and additional information, we refer the interested reader to Holzapfel (2000). We further decompose the deformation gradient F_e into volumetric F_e^{vol} and volume-preserving (isochoric) F_e^{iso} parts,

$$F = F_e^{\text{vol}} \cdot F_e^{\text{iso}}$$
where $F_e^{\text{iso}} = J_e^{-1/3} F_e$ and $F_e^{\text{vol}} = J_e^{1/3} I$, (5)

with the determinant $J_e = [\lambda_e]_1 [\lambda_e]_2 [\lambda_e]_3$. Thus, the Ogdentype free energy splits into isochoric and volumetric parts (Ogden 1973; Reese and Govindjee 1998; Nedjar 2016)

$$\Psi_{\text{NEQ}} = \Psi_{\text{NEQ}}^{\text{iso}} + \Psi_{\text{NEQ}}^{\text{vol}}$$
with
$$\Psi_{\text{NEQ}}^{\text{iso}} = \sum_{i=1}^{3} \frac{\mu_{\nu}}{\alpha_{\nu}} \left[[b_{e}^{\text{iso}}]_{i}^{\alpha_{\nu}/2} - 1 \right]$$
and
$$\Psi_{\text{NEQ}}^{\text{vol}} = \frac{3}{8} \kappa_{\nu} \left[J_{e}^{4/3} + 2J_{e}^{-2/3} - 3 \right],$$
(6)

where the $[b_e^{\text{ iso }}]_i = J_e^{-2/3} [b_e]_i$ and $[b_e]_i = [\lambda_e]_i^2$.

Using (6), the principal Kirchhoff overstresses are given by

$$\begin{split} \left[\tau_{\text{NEQ}}\right]_{i} &= \left[\tau_{\text{NEQ}}^{\text{iso}}\right]_{i} + \tau_{\text{NEQ}}^{\text{vol}} \quad \text{where} \\ &\left[\tau_{\text{NEQ}}^{\text{iso}}\right]_{i} = \sum_{j=1}^{3} \frac{\partial \Psi_{\text{NEQ}}^{\text{iso}}}{\partial \left[b_{e}^{\text{iso}}\right]_{j}} \frac{\partial \left[b_{e}^{\text{iso}}\right]_{j}}{\partial \left[\lambda_{e}\right]_{i}} \left[\lambda_{e}\right]_{i} \\ \text{and} \quad \tau_{\text{NEQ}}^{\text{vol}} &= \frac{\partial \Psi_{\text{NEQ}}^{\text{vol}}}{\partial I} J_{e} \,. \end{split} \tag{7}$$

The overstresses $[\tau_{\text{NEQ}}]_i$ vanish at the thermodynamic equilibrium. This viscous effect in the structural behavior is linked to the internal strain variable, i.e., the inverse of the viscous part of the Cauchy-Green tensor $C_v^{-1} = \underline{F}^{-1} \cdot b_e \cdot F^{-T}$. Using the Lie derivative $\mathcal{L}_v b_e = F \cdot \overline{C_v^{-1}} \cdot F^T$, the evolution equation can be defined

$$-\frac{1}{2}(\mathcal{L}_{\nu}\boldsymbol{b}_{e})\cdot\boldsymbol{b}_{e}^{-1}=\boldsymbol{v}^{-1}:\boldsymbol{\tau}_{\text{NEQ}},$$
(8)

and the fourth-order tensor v^{-1} is isotropic and positive-definite (Reese and Govindjee 1998)

$$\mathbf{v}^{-1} = \frac{1}{2\eta_{\text{dev}}} (\mathbb{I} - \frac{1}{3}\mathbf{I} \otimes \mathbf{I}) + \frac{1}{6\eta_{\text{vol}}} (\mathbf{I} \otimes \mathbf{I}), \tag{9}$$

with volumetric and shear viscosities η_{vol} and η_{dev} , respectively, and the associated relaxation time(s)

$$\tau = \frac{\eta_{\text{vol}}}{K_{v}} = \frac{\eta_{\text{dev}}}{(\mu_{v}\alpha_{v})}.$$
 (10)

The details on the finite element implementation and the solution of the evolution equation can be found in Reese and Govindjee (1998). One contribution of this paper is to formulate finite viscoelasticity integrated with non-local damage, detailed in the next section.

2.1.2 Non-local damage formulation

Considering the damage to the material, we define the local free energy function accounting for the nonlinear viscoelastic material response as

$$\Psi = \Psi_{\text{loc}}(\boldsymbol{C}, \boldsymbol{F}_{v}, \kappa) = f_{d}(\kappa) \Psi_{\text{EQ}}(\boldsymbol{C}) + f_{d}(\kappa) \Psi_{\text{NEO}}(\boldsymbol{F}_{v}^{-T} \cdot \boldsymbol{C} \cdot \boldsymbol{F}_{v}^{-1}),$$
(11)

where $f_d(\kappa) \in (0,1]$ is the scalar damage function and $\kappa \in [0,\infty)$ is the non-decreasing local damage (internal) variable, i.e., $f_d(0){=}1$ (no damage) and $\lim_{\kappa \to \infty} f_d(\kappa) = 0$ (fully damaged). For the damage function, we consider an exponential form $f_d(\kappa){=}\exp(\eta_d[\kappa_d-\kappa])$ among other alternatives (Waffenschmidt et al. 2014). The damage initiation threshold κ_d should be exceeded to activate the damage evolution, which is further defined using the damage saturation rate η_d , see (Waffenschmidt et al. 2014) for further detail. The evolution Eq. (8) is extended to account for the damage function as

$$-\frac{1}{2}(\mathcal{L}_{\mathbf{v}}\boldsymbol{b}_{e})\cdot\boldsymbol{b}_{e}^{-1} = \mathbf{v}^{-1}: f_{d}(\kappa)\boldsymbol{\tau}_{\text{NEQ}}. \tag{12}$$

Introduction of the non-local free energy ψ_{nloc} regularizes the damage over the volume through a non-local gradient term and a penalty term

$$\Psi_{\text{nloc}} = \Psi_{\text{nloc}}(C, \phi, \nabla_X \phi, \kappa) = \underbrace{\frac{c_d}{2} \nabla_X \phi \cdot C^{-1} \cdot \nabla_X \phi}_{\Psi_{\text{nloc}}^{\text{grad}}} + \underbrace{\frac{\beta_d}{2} \left[\phi - \kappa \right]^2}_{\Psi_{\text{nloc}}^{\text{penalty}}}, \tag{13}$$

where c_d is the gradient regularization (length scale) parameter and ϕ is the non-local damage field that is directly linked to the local damage κ using the penalty parameter $\beta_d = 200$ kPa⁻¹. Overall, the resulting gradient-enhanced free energy potential becomes $\Psi = \Psi_{\text{loc}} + \Psi_{\text{nloc}}$. For the given form of



the free energy contributions (6) and (13), the coupled governing equations are given in the following section.

2.1.3 Coupled governing equations

The coupled Euler-Lagrange equations can be derived from the stationary conditions of a minimization principle. Here, again, we point the interested reader to excellent work for more details, see (Ostwald et al. 2019) for example. The resulting weak forms of the balance of linear momentum and the governing equation for the non-local damage field are

$$\int_{\mathcal{B}_{t}} \boldsymbol{\tau} : \nabla_{x} \delta \boldsymbol{\varphi} \, dV = 0$$

$$\int_{\mathcal{B}_{t}} c_{d} \nabla_{x} \cdot (\nabla_{x} \boldsymbol{\phi}) \delta \boldsymbol{\phi} \, dV + \int_{\mathcal{B}_{t}} \beta_{d} (\boldsymbol{\phi} - \kappa) \delta \boldsymbol{\phi} \, dV = 0 \tag{14}$$

respectively, in the absence of body forces in the volume and traction forces on the surface. We further assume zero-flux conditions for the damage field on the entire boundary.

2.2 Mixed isogeometric discretization

The weak forms of the coupled governing equations (14) are discretized using B-splines in the context of isogeometric analysis (Hughes et al. 2005; Cottrell et al. 2009; Bazilevs et al. 2006). Consider a knot vector $\Xi = \{\xi_1, \xi_2, \dots, \xi_{n+p+1}\}$, a sequence of n+p+1 non-decreasing (sorted) numbers, where p is the degree of polynomial and n is the number of basis functions. Given the knot vector Ξ , B-spline basis functions are defined starting with piecewise constants (p=0)

$$N_{i,0}(\xi) = \begin{cases} 1 & \text{if } \xi_i \le \xi < \xi_{i+1} \\ 0 & \text{otherwise} \end{cases}$$
 (15)

and recursively calculated for higher orders ($p \ge 1$) using

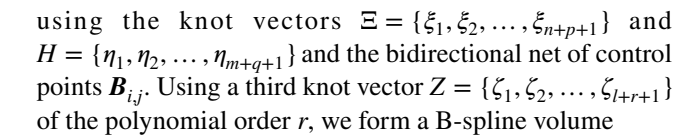
$$N_{i,p}(\xi) = \frac{(\xi - \xi_i)N_{i,p-1}(\xi)}{\xi_{i+p} - \xi_i} + \frac{(\xi_{i+p+1} - \xi)N_{i+1,p-1}(\xi)}{\xi_{i+p+1} - \xi_{i+1}}.$$
 (16)

A B-spline curve of degree p can be represented in \mathbb{R}^d as the linear combinations of the basis functions $N_{i,p}$

$$\mathscr{C}(\xi) = \sum_{i=1}^{n} N_{i,p}(\xi) \boldsymbol{B}_{i}, \qquad (17)$$

using the control points B_i , i=1,2,...,n. B-spline geometries in higher dimensions can be formed using tensor products of univariate B-spline basis functions. For example, a B-spline surface $\Gamma(\xi,\eta)$ is obtained

$$\Gamma(\xi, \eta) = \sum_{j=1}^{m} \sum_{i=1}^{n} N_{i,p}(\xi) N_{j,q}(\eta) \mathbf{B}_{i,j}$$
(18)



$$\mathbf{\Omega}(\xi, \eta, \zeta) = \sum_{k=1}^{l} \sum_{i=1}^{m} \sum_{i=1}^{n} N_{i,p}(\xi) N_{j,q}(\eta) N_{k,r}(\zeta) \mathbf{B}_{i,j,k}$$
(19)

with a 3D grid of control points $B_{i,i,k}$.

For our numerical calculations the computational domain is discretized by \mathcal{C}^1 -continuous B-spline volume elements, where solid deformations and the non-local damage variable are independently approximated

$$\varphi \approx \varphi^h = N^{\varphi}(\xi)\varphi$$
 and $\varphi \approx \varphi^h = N^{\varphi}(\xi)\varphi$ (20)

using the same B-spline basis functions, i.e., $N^{\varphi}=N^{\phi}$. The choice of the same basis functions is due to its computational efficiency and the mixed interpolation spaces do not have to coincide, e.g., see (Waffenschmidt et al. 2014).

2.3 Specimen preparation

We created blood clots from bovine blood that we obtained from a commercial service (Lampire Biological Laboratories, PA, USA). The blood was collected by directly bleeding into anticoagulant (CPDA-1 anticoagulant at 14% volume/ volume) before it was shipped overnight and stored for less than 48 hours in our laboratory at 4 °C. To coagulate, i.e., polymerize, blood we added calcium chloride to a final concentration of 20 mM to reverse the anticoagulant (Sugerman et al. 2020a, b). Immediately after adding calcium chloride, we injected the coagulating blood into a 2-piece mold that was lined with hook-and-loop fabric on two sides, see Fig. 1a. In turn, the mold had two sliding attachments so it could be easily attached to our table top Instron uniaxial tensile testing machine (Instron 5942, 10N capacity, 20mN accuracy, Norwood, MA, USA). This technique requires no clamping or gluing of the sample and thus avoids unnecessary damage or altering the material through exposure to the glue. As previously described, the samples were given 60 minutes to fully coagulate before experiments were quickly commenced. Note, in our previous work, we found no significant effect of coagulation time between 60 and 120 minutes on the mechanics of blood clots (Sugerman et al. 2020a).

2.4 Mechanical testing

Once we mounted the samples to our tensile testing machine we conducted one of three protocols: (i) cyclic loading to successively increasing strain (by increments of 10% clampto-clamp strain) until failure at a rate of 0.01 mm/s, (ii)



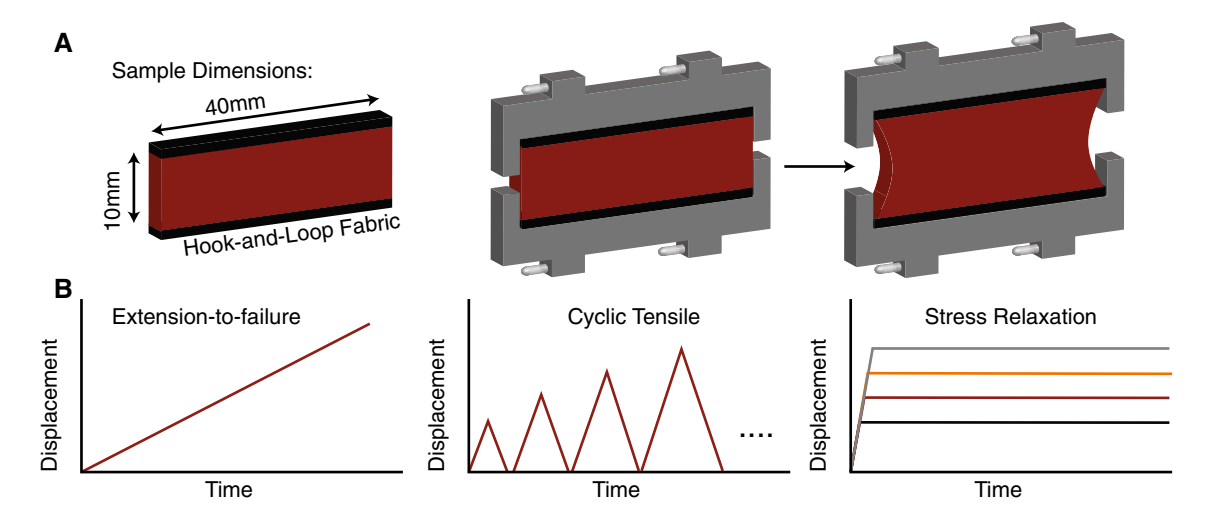


Fig. 1 Sample dimensions and loading protocols. a We coagulated samples between two mold pieces that we separated during testing. b Three mechanical loading protocols used for parameter identification and model validation

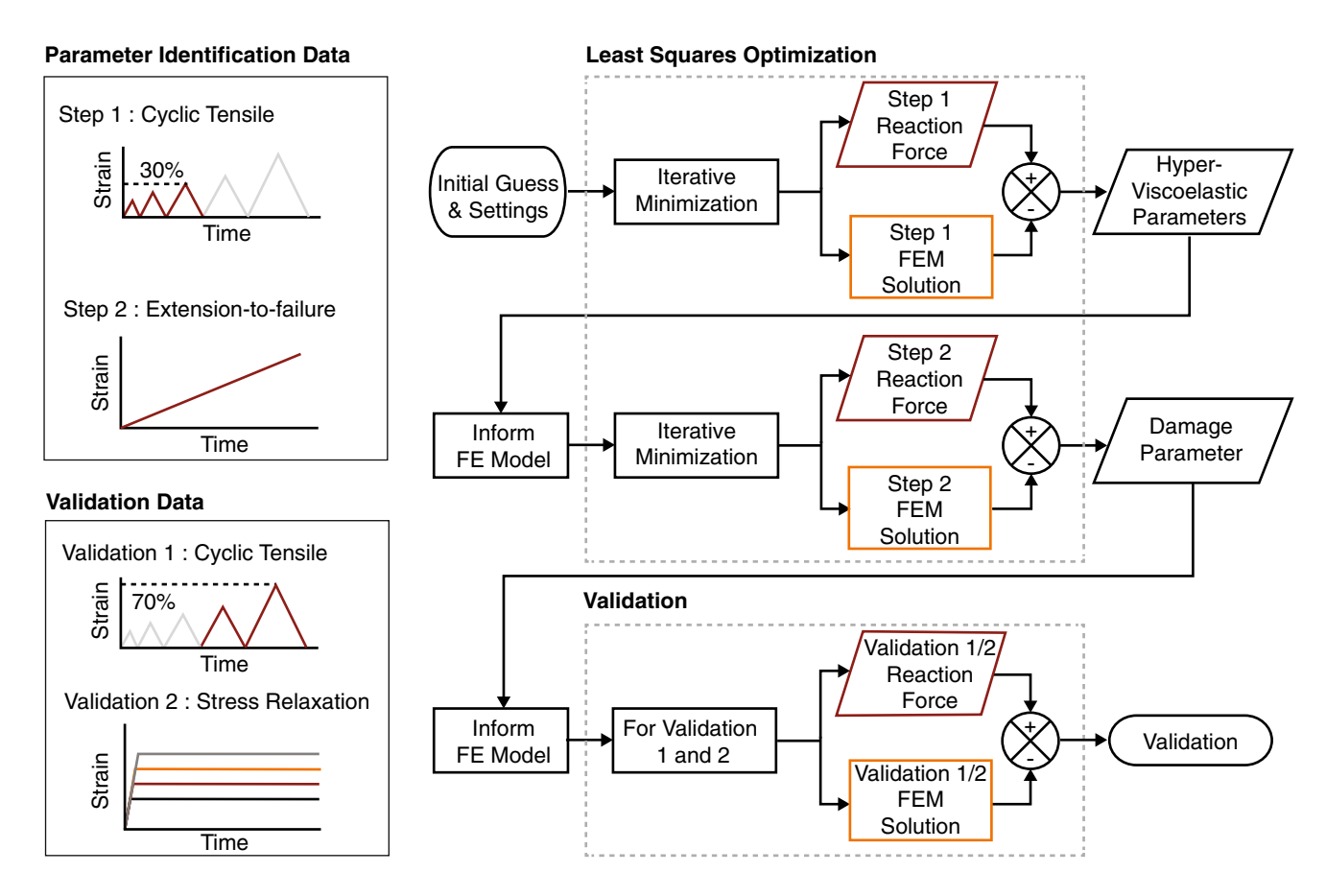


Fig. 2 Inverse finite element algorithm and validation steps. For the parameter identification, we identified the hyper-viscoelastic parameters in Step 1, for which we used the cyclic tensile tests up to 30% strain. Note, we assumed that no damage had been accrued up to this strain. In Step 2, we used the extension-to-failure data to inform the damage parameter, while keeping the hyper-viscoelastic parameters

from the previous step fixed. Upon informing all model parameters, we conducted validation experiments in which we predicted the response to unseen cyclic tensile tests data at strains larger than 30% (Validation 1). Additionally, we compared our predicted response to stress relaxation experiments to four different strain levels (Validation 2)



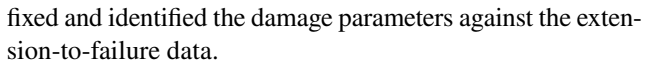
uniaxial extension-to-failure tests at 0.01 mm/s, and (iii) stress-relaxation tests during which we displaced the samples at a rate of 0.01 mm/s to either 10%, 20%, 30%, or 40% clamp-to-clamp strain followed by a 300 s hold, see Fig. 1b. Before each experiments, we displaced the samples by 0.5 mm to separate the clamps and all experiments were conducted in physiological solution at 37 °C. Note, we chose the displacement rate of 0.01 mm/s as the fastest displacement rate that did not result in visible inertial effects and device backlash.

2.5 Inverse finite element parameter identification

We used an inverse finite element approach to identify the nine parameters to our proposed hyper-viscoelastic damage model of blood clots, see Fig. 2. Specifically, we identified the two parameters governing the hyperelastic Ogden model, $\bar{\mu}_{e}$ and $\bar{\alpha}_{e}$, six parameters governing the viscoelastic response of the material, the viscoelastic parameters $\bar{\mu}_{v,k}$, $\bar{\alpha}_{v,k}$, and the relaxation times τ_k for $k = \{1, 2\}$, and one of the three damage parameters, the saturation rate η_d . In contrast, we fixed the damage initiation threshold κ_d to 0.28 kPa (corresponding to approximately 30% overall strain) and regularization parameter c_d to 500 kPa⁻¹· mm² in the absence of experimental data relating to these parameters (discussion to follow). Note, we assumed a nearly incompressible material behavior for blood clots and adopted the relation between the Lame parameters as $\lambda = 50\mu$. Please note, blood clots' highly hydrated nature could allow for significant volume changes as extreme deformations may lead to fluid expulsion. However, under visual inspection, we did not see such affects in our experiments and thus adhere to the convention of modeling blood clots as incompressible. During the inverse identification, we used a heuristic optimization technique that calls forward finite element solutions of the uniaxial tensile experiments and iteratively minimizes following objective function, which represents the difference between measured and calculated reaction force:

$$f_{obj} = \sum_{t} |F^{\text{exp}} - F^{\text{sim}}(\boldsymbol{X})|^2, \qquad (21)$$

where X is the vector of unknown parameters and t is the discrete time points at which we sampled our data and evaluated our model. To decouple the hyper-viscoelastic response from the damage response, we conducted this inverse identification in two steps. In the first step, we identified the hyper-viscoelastic parameters using the cyclic tensile tests up to 30% strain only. Note, here, we assumed that no or little damage occurs below 30% strain. Once those parameters were identified, in a second step, we kept those parameters



Taking advantage of the symmetry of our specimen geometry and of the loading conditions, we only simulated an eighth of the specimen. We discretized this geometry and the coupled governing Eq. (14) using quadratic C^1 -continuous B-spline elements and solved the ensuing boundary value problem using a custom, implicit nonlinear isogeometric finite element software in which we solved the coupled nonlinear system incrementally using the iterative Newton–Raphson method with the direct sparse solver Pardiso (Alappat et al. 2020; Bollhöfer et al. 2019).

3 Results

3.1 Local versus non-local damage modeling

In our current work, we chose to implement a gradientenhanced, non-local damage formulation (Ostwald et al. 2019; Waffenschmidt et al. 2014). Figure 3a, b illustrates a key feature of this implementation: Once converged, this formulation is mesh-independent. In other words, the accrued damage is not a function of the chosen spatial discretization. Specifically, in Fig. 3a, we compare both h- and p-refined discretizations. That is, we increase the total number of elements ranging from 'coarse' (200 elements) to 'finer' (3600 elements). Additionally, we increase the order of the interpolation scheme from linear (Q1Q1) to quadratic (Q2Q2). Clearly, both refinements lead to a converged solution. Similarly, Fig. 3b shows that the damage variable, f_d , also converges with both refinements. In contrast, Fig. 3c, d shows the identical convergence analysis for a local formulation. While the solution with the local damage implementation appears to converge, i.e., the curves for h- and p-refined meshes appear to collapse, the simulations fail prematurely (indicated by blue 'x'), Fig. 3c. Additionally, Fig. 3d illustrates non-convergence of the damage variable, f_d .

3.2 Hyper-viscoelastic parameter identification

In a first step, we identified the hyper-viscoelastic material parameters against cyclic tensile tests up to 30% clamp-to-clamp strain. See Fig. 4 for photographs of a representative test sample in the reference configuration (a) and the deformed configuration at 6 mm clamp displacement (b). The experimental data and our optimal fit are shown in Fig. 5. Experimentally, we see that the material shows negligible nonlinearity as well as set after the first and second loading to 10% and 20% clamp-to-clamp strain, respectively. This behavior is consistent with our previous reports on the nonlinear mechanics of blood clots (Sugerman et al. 2020a).



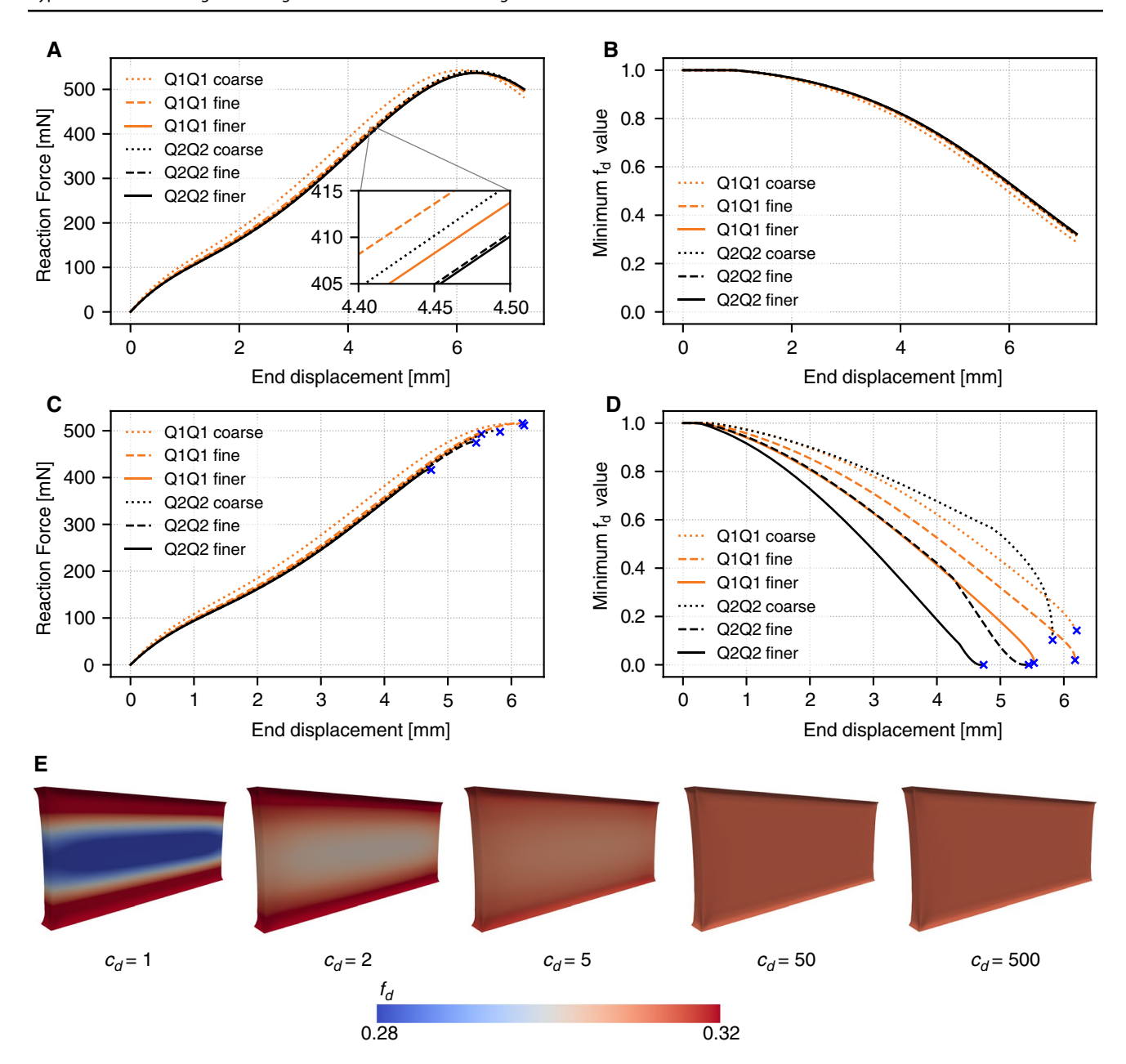


Fig. 3 Non-local damage formulation converges for both h- and p-refinement, while a local damage formation does not. **a** With increasing element number (h-refinement) and with increasing interpolation order (p-refinement), the predicted solutions begin to overlap. Note, the 'coarse' mesh has 200 elements, the 'fine' mesh has 1200 elements, and the 'finer' mesh has 3600 elements. **b** The damage variable $f_{\rm d}$ also converges for both types of refinement. **c** The solution fails prematurely and does not converge for either increas-

ing element number (h-refinement) or increasing interpolation order (p-refinement). **d** Non-convergence of the local damage approach is even more evident for the damage variable $f_{\rm d}$ which varies widely between h- and p-refinement levels. **e** Example of a representative simulation ('finer' mesh and Q2Q2 formulation) with a comparison of different c_d values which serves as a length-scale, where a lower value corresponds to a more localized damage zone. Note, we fixed κ_d to 0.28 kPa and c_d to 500 kPa⁻¹·mm² during our simulations

Our model fit reflects this behavior accurately with the only discrepancy stemming from our model exhibiting higher nonlinearity than our experimental findings. We report the identified hyperelastic Ogden parameters, $\bar{\mu}_e$ and $\bar{\alpha}_e$, and viscoelastic parameters, $\bar{\mu}_{v,k}$, $\bar{\alpha}_{v,k}$, τ_k for $k = \{1,2\}$ in Table 1.

3.2.1 Damage parameter identification

In a second step, we identified the damage parameters against uniaxial extension-to-failure tests. Note, for these fits, the hyper-viscoelastic parameters identified in the previous step remained unchanged. The experimental data



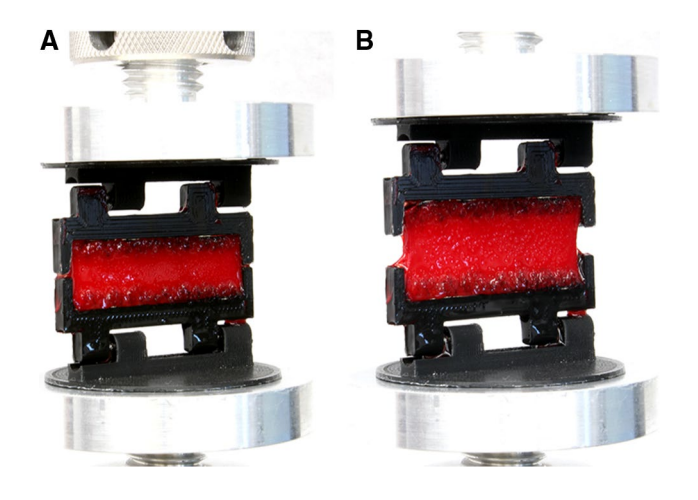


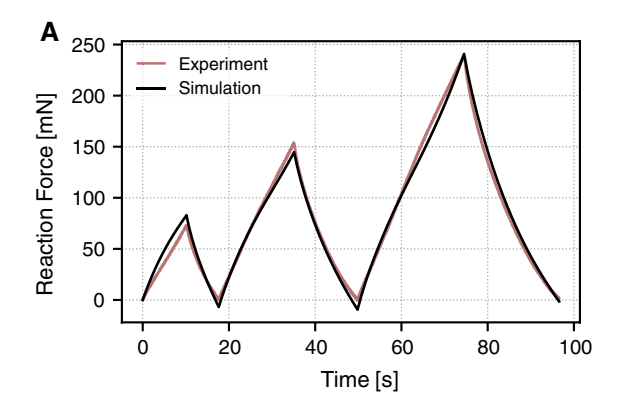
Fig. 4 Photographs of representative sample during tensile testing. **a** Sample in the undeformed configuration. **b** Sample in the deformed configuration at 6mm clamp displacement. Note, for visualization, these images were taken without the fluid bath

and our optimal fit are shown in Fig. 6. Experimentally, we see that the material, again, shows negligible nonlinearity until failure which appears abruptly at approximately 70% clamp-to-clamp strain. This behavior is consistent with our previous reports and our cyclic tensile test data (Sugerman et al. 2020a). Our model fit (with damage)

reflects the extension-to-failure data accurately with the only discrepancy stemming from our model, again, exhibiting higher nonlinearity than our experimental findings. This discrepancy does not stem from our model's general inability to fit these data, but from a competition between two independently collected data sets with global parameters. We illustrate this assertion by fitting our full model to the extension-to-failure test data independently. These independent fits are almost perfect, see Supplementary Figure & Table 1 (see Online Resource 1). Additionally, to compare fitting with and without damage in Fig. 6a, we also super-imposed our model fit without damage based on the parameters identified in the previous step (light gray). This superposition demonstrates that both fits show excellent agreement up to 30% clamp-to-clamp strain supporting our assumption that no (or little) damage occurs prior but deviate significantly beyond 30%. Figure 6b illustrates the damage variable, f_d , corresponding to the simulation with damage in Fig. 6a.

3.3 Validation 1—cyclic tensile tests

In a first test of our model's ability to predict, we compared our predictions to cyclic tensile tests with increasing magnitude up to 70% clamp-to-clamp strain (see Fig. 7a, b).



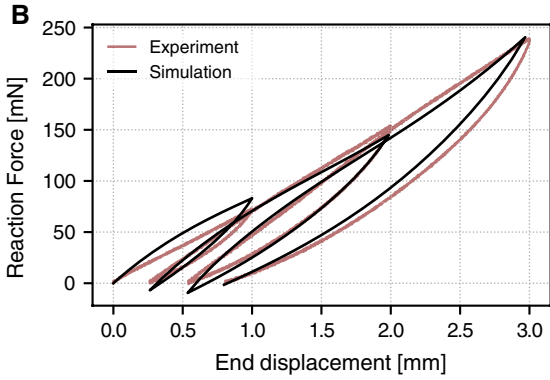


Fig. 5 Blood clots' mechanics show viscoelastic behavior up to 30% clamp-to-clamp strain, which is well captured by our hyper-viscoelastic framework without inclusion of damage. **a** Force-time evolution of our tensile cyclic test with increasing magnitude. Our hyper-viscoelastic model fits our experimental data both qualitatively and quantitatively. **b** Force-displacement evolution of the same experi-

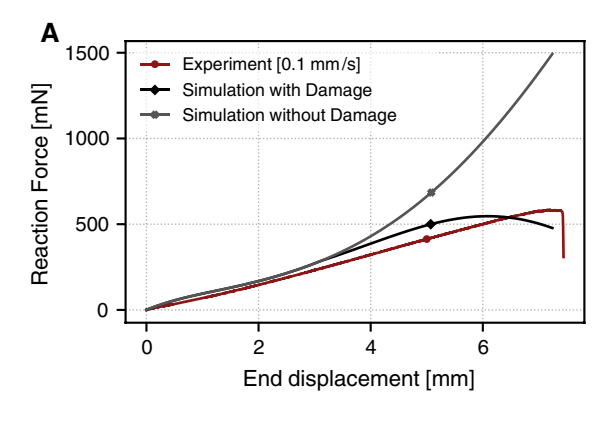
mental data as in **a** demonstrate set and hysteresis, which are both captured well by our hyper-viscoelastic framework without inclusion of damage. Note, for these simulations, we used the 'finer' mesh with quadratic shape functions. The parameters of this fit are reported in Table 1

Table 1 Optimal parameters of our hyper-viscoelastic model without inclusion of damage.

$\bar{\mu}_e$ [kPa]	$\bar{\alpha}_e^{}\left[-\right]$	$\bar{\mu}_{v,1}$ [kPa]	$\bar{\alpha}_{v,1}[-]$	$\tau_1[s]$	$\bar{\mu}_{v,2}$ [kPa]	$\bar{\alpha}_{v,2}\left[-\right]$	$\tau_2[s]$
0.22468	8.59846	0.18373	18.06303	6.76230	0.70799	0.84515	168.44204

 $\bar{\mu}_e$ and $\bar{\alpha}_e$ are the Ogden parameters of the hyperelastic model, while all other parameters belong to the viscoelastic terms in our model





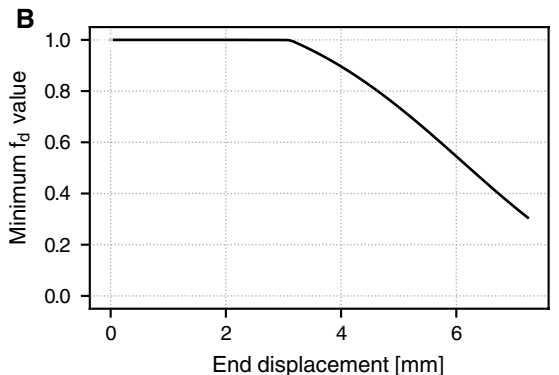


Fig. 6 Blood clots' mechanics show mostly linear behavior until failure at approximately 70% clamp-to-clamp strain, which is captured well by our hyper-viscoelastic damage model. **a** Our simulations with damage are well-aligned with our experimental data. Additionally, we

superimposed our hyper-viscoelastic model without damage for reference. **b** Shows the damage variable $f_{\rm d}$, which does not begin accruing up to a clamp-to-clamp strain of approximately 30%. We identified the optimal damage parameter $\eta_{\rm d}=0.46720$

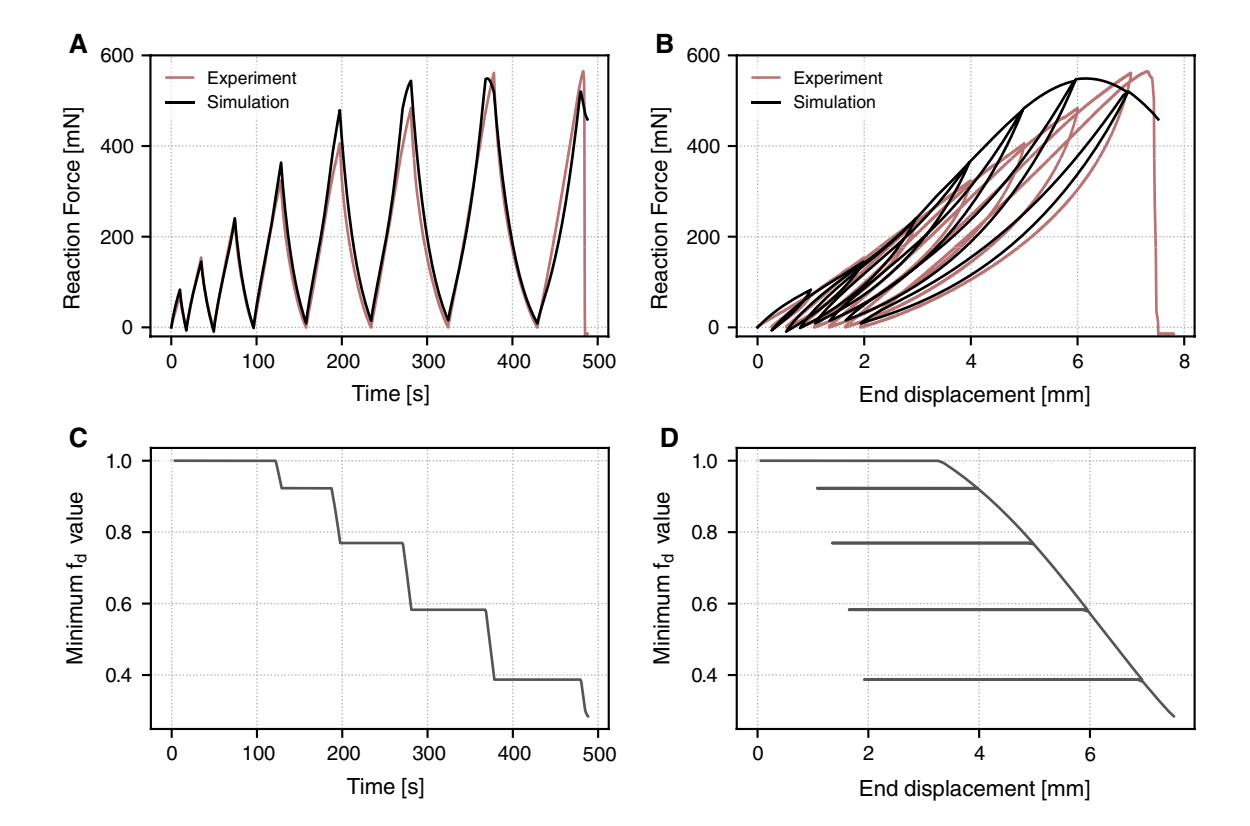


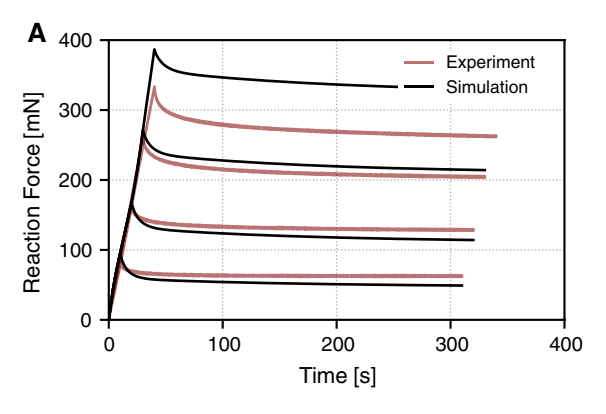
Fig. 7 Our hyper-viscoelastic damage model accurately predicts previously left out cyclic tensile data up to 70% clamp-to-clamp strain. **a** Our model fits the force-time data both qualitatively and quantitatively very accurately. **b** The force-displacement data highlight some

deviations between our predicted response and the experimental finding by overestimating the force magnitude with increasing strain. ${\bf c}$ The evolution of $f_{\rm d}$ corresponding to (${\bf a}$). ${\bf d}$ The evolution of $f_{\rm d}$ corresponding to (${\bf b}$)

Note, we used a subset of these data (up to 30% clamp-to-clamp strain) to fit our hyper-viscoelastic parameters in Sect. 3.2. The corresponding strain-time evolution of the damage variable, $f_{\rm d}$, is shown in Fig. 7c, d. Figure 7a demonstrates excellent agreement between our experiments and

our predictions of the force-time behavior. When displaying the same data as force-displacement, some discrepancies are notable. Specifically, at larger clamp-to-clamp strain, our model overestimates the total force. However, the average prediction error of approximately 18% falls well within the





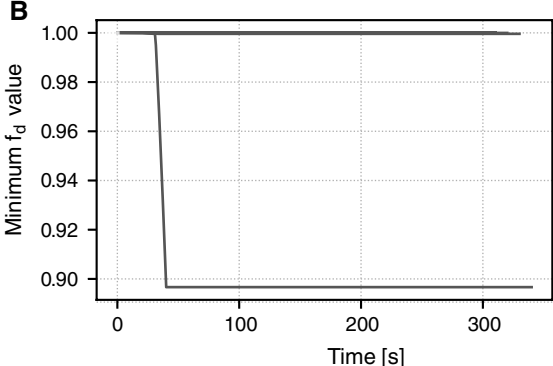


Fig. 8 Our hyper-viscoelastic damage model generally predicts unseen stress-relaxation data. **a** Our model fits our experimental measurements fairly well. That is, significant deviations between the

measured and predicted equilibrium forces can be observed. ${\bf b}$ The corresponding evolution of $f_{\rm d}$

measurement error of these type of experiments, see our previous work for comparison (Sugerman et al. 2020a, b). Additionally, the predicted failure is less abrupt, i.e., more ductile, than our experimental findings. This difference is likely due to singular nature of the fracture nucleation, which we do not capture with our continuum model.

3.4 Validation 2—stress relaxation tests

In a second test of our model's ability to predict, we compared our predictions to entirely 'unseen' stress-relaxation tests. In other words, these data were not used at all during the fitting procedure (see Fig. 8). Figure 8a demonstrates good agreement between our experiments and our predictions of the force-time behavior. The corresponding evolution of the damage variable, f_d , is shown in Fig. 8b. While there are clear discrepancies between the predictions and the experiments, we note that the average error between predicted and measured forces is only 13.6%, which is comparable to between-sample variations previously reported (Sugerman et al. 2020a, b). Again, we note that discrepancies between experiments and model predictions do not stem from our model's inability to capture the stress-relaxation behavior, in general, but from a global fit of four independent stress-relaxation tests that suffer from between-specimen variability. To support this assertion, we also fit our model to each stress-relaxation data independently as shown in Supplementary Figure & Table 2 (see Online Resource 1).

4 Discussion

We have previously reported on the mechanics of blood clots and demonstrated that blood clots exhibit strain-rate dependence, hysteresis, a Mullin's-like damage, nonlinear stress-relaxation, and set (Sugerman et al. 2020a, b). In

other words, blood clots are classic viscoelastic materials. Acknowledging and understanding its viscoelasticity are not only important to our basic understanding of blood clots, but also critical to the development of computational methods for diagnosis, prognosis, and therapy of thrombotic diseases.

Our experimental findings in this current work reflect those of previous investigations including our own (Johnson et al. 2017). Specifically, we found that blood clots show all signs of a nonlinear, viscoelastic material. In our first set of experiments, cyclic loading with increasing magnitude, blood clots showed hysteresis, a Mullin's-like damage phenomenon, and set (Rausch and Humphrey 2016, 2017). Note that, "set" likely includes a temporary, i.e., viscoelastic, and permanent, i.e., plastic, contribution. The extent to which blood clots are therefore a viscoplastic rather than viscoelastic material will have to be studied in more detail. Additionally, we showed that blood clots undergo very large deformation before failure (up to 70%) in our extension-tofailure experiments, and nonlinear stress-relaxation in our stress-relaxation experiments (Tutwiler et al. 2020; Fereidoonnezhad et al. 2020).

To cast above experimental findings into a comprehensive constitutive framework, we brought together a hyperelastic constitutive law that has previously been demonstrated to excellently represent blood clots of various origin (Ogden 1973; Sugerman et al. 2020a), a well-established viscoelastic model (Reese and Govindjee 1998), and a gradient-enhanced damage formulation (Waffenschmidt et al. 2014; Ostwald et al. 2019). We first illustrated the importance of a non-local damage approach by contrasting it to a local approach, before fitting our hyper-viscoelastic damage model to original data on blood clots' mechanics. Our comparison between the two formulations confirmed that only a non-local damage approach ensures mesh-independence, while the local approach was (i) unstable in that simulations failed prematurely, and (ii) showed mesh-dependence. While this



is a known phenomenon that has been investigated by the mechanics community (De Vree et al. 1995), the wider biomechanics community continues to use local approach likely owing to its simple implementation and wide availability in open- and commercial finite element software. We hope that our findings provide additional impetus to leave local damage approaches behind and focus on non-local approaches.

When fit to our experimental data, our constitutive framework fit our data well, albeit not perfect. Specifically, our fits to extension-to-failure data deviated in that they demonstrated a higher degree of nonlinearity when compared to the experiments. It is important to keep in mind that deviations are not inherent to the framework, but due to simultaneous fits to both cyclic tensile data and extension-to-failure data. We demonstrated this assertion in our supplementary materials. Finally, we validated our fits against two sets of unseen data: (i) cyclic tensile test data at larger strains than used during the parameter identification, (ii) and entirely unseen stress-relaxation data. Here again, we achieved good, but imperfect fits. Naturally, we would have liked to see better fits, which would likely be possible with more complex models, accounting for plastic deformations and poroelastic behaviors. However, we must keep in mind that the observed errors fell well within our measurement uncertainty. Additionally, our goal was to introduce a comprehensive, yet practical, i.e., computationally tangible, model, which we believe we achieved. Please see Supplementary Table 3 (Online Resource 1) for a summary of all fit and validation errors. As to the interpretation of our model parameters: While we chose a mostly phenomenological approach, each parameter class has a clear physical meaning. That is, the hyperelastic Ogden parameters are associated with the material's equilibrated response, i.e., after all viscous effects have dissipated. Consequently, the non-equilibrium parameters are associated with those phenomena that are temporary, likely driven by solid-viscoelastic effects and poroelastic effects due to intra- and inter-porous fluid flow. Finally, the damage parameters are associated with the accumulation of macro- and/or microscopic flaws in the material that reduce the ability of the material to store strain-energy.

Also note, while fibrin is a constituent of blood clots and undoubtedly plays an important role in determining its mechanical behavior, fibrin and blood clots are vastly different materials. In contrast to pure fibrin, blood clots contain active and passive formed elements, platelets and red blood cells, and a myriad of other plasma-borne factors. The addition of these formed elements alters the mechanics of blood clots significantly (Gersh et al. 2009; Lam et al. 2011; Kim et al. 2017; van Oosten et al. 2019). For this reason, we have specifically abstained from including and discussing the important and excellent previous work on multi-scale fibrin mechanics (Münster et al. 2013; Janmey et al. 1983;

Brown et al. 2009; Piechocka et al. 2010; Weisel 2004; Liu et al. 2006; Kim et al. 2016; Wang et al. 2020).

Finally, our work was and is subject to limitations. For example, our fits and validation are limited to measurements of clamp-to-clamp displacement/strain and reaction force. Ideally, we would have included some experimental quantification to validate our ability to predict damage. Unfortunately, to the best of our knowledge, there are no reliable means to visualize and/or quantify mechanical damage in blood clots. While there have been recent developments of collagen-specific mechanical damage visualization probes (Zitnay et al. 2017), none are available for fibrin. Thus, including quantification of mechanical damage in blood clots remains subject to future studies. As a consequence of this limitation, we did not have means to determine at what strain mechanical damage began to accrue. For our fitting of the damage-independent, hyper-viscoelastic parameters, we chose cyclic loading data at less than 30%, assuming that no or little damage accrues before then. This decision was based on pilot experiments in which repeated loading to 10, 20, and 30% strain did not appear to yield significant changes to the constitutive behavior of blood clots. Similarly, we had no means to inform/fit c_d . Instead, we chose c_d to yield homogeneous damage fields, an assumption which will have to be tested in the future. Yet another limitation is the age of our blood. While we test blood within 72 hours of receipt and have shown that mechanical properties of blood clots do not significantly change during this time (Sugerman et al. 2020a, b), we suspect that platelet activity may be reduced at the time of testing. Future work on human blood that can be tested immediately after being drawn may enable controlled studies in which platelets could be deactivated via addition of blebbistatin—a myosin-II inhibitor—for example. Finally, we treat our material as isotropic. While we are confident that stress-free blood clots are isotropic, we have not tested whether blood clots exhibit deformationinduced anisotropy. In our future work, we will make use of our recently introduced in situ imaging protocols to quantify deformation-induced anisotropy and will thus overcome this current limitation (Wang et al. 2020).

In conclusion, we introduced original data on blood clots' mechanics and a comprehensive hyper-viscoelastic damage model to cast the complex, nonlinear, viscoelastic behavior of blood clots into a constitutive form. We found good agreement between our model predictions and unseen, test data. Our model and model data will be useful for basic understanding of blood clots' physiology and for predictive modeling of thromboembolic disease.

Supplementary Information The online version contains supplementary material available at https://doi.org/10.1007/s10237-021-01467-z.



Acknowledgements This work was supported by the University of Texas at Austin William's Excellence Award and by the National Science Foundation under Award BMMB-2046148. Dr. Rausch also discloses a financial relationship to Edwards Lifesciences. We also thank our colleague Dr. Sapun Parekh for his editorial help.

Data Availability Statement Data are made available on the Texas Data Repository under https://dataverse.tdl.org/dataverse/Clothyperviscod amagedata.

References

- Alappat C, Basermann A, Bishop AR, Fehske H, Hager G, Schenk O, Thies J, Wellein G (2020) A recursive algebraic coloring technique for hardware-efficient symmetric sparse matrix-vector multiplication. ACM Trans Parallel Comput (TOPC) 7(3):1–37
- Bazilevs Y, Beirao da Veiga L, Cottrell J.A, Hughes T.J, Sangalli G (2006) Isogeometric analysis: approximation, stability and error estimates for h-refined meshes. Math Models Methods Appl Sci 16(07):1031–1090
- Bollhöfer M, Eftekhari A, Scheidegger S, Schenk O (2019) Large-scale sparse inverse covariance matrix estimation. SIAM J Sci Comput 41(1):A380–A401
- Brown AEX, Litvinov RI, Discher DE, Purohit PK, Weisel JW (2009) Multiscale mechanics of fibrin polymer: gel stretching with protein unfolding and loss of water. Science 325(5941):741–4
- Cines DB, Lebedeva T, Nagaswami C, Hayes V, Massefski W, Litvinov RI, Rauova L, Lowery TJ, Weisel JW (2014) Clot contraction: compression of erythrocytes into tightly packed polyhedra and redistribution of platelets and fibrin. Blood 123(10):1596–603
- Cottrell JA, Hughes TJ, Bazilevs Y (2009) Isogeometric analysis: toward integration of CAD and FEA. Wiley, Hoboken
- De Vree J, Brekelmans W, Van Gils M (1995) Comparison of nonlocal approaches in continuum damage mechanics. Comput Struct 55(4):581–588
- Di Martino E, Mantero S, Inzoli F, Melissano G, Astore D, Chiesa R, Fumero R (1998) Biomechanics of abdominal aortic aneurysm in the presence of endoluminal thrombus: experimental characterisation and structural static computational analysis. Eur J Vasc Endovasc Surg 15(4):290–299
- Esmon CT (2009) Basic mechanisms and pathogenesis of venous thrombosis. Blood Rev 23:225-9
- Fereidoonnezhad B, Dwivedi A, Johnson S, McCarthy R, McGarry P (2021) Blood clot fracture properties are dependent on red blood cell and fibrin content. Acta Biomaterialia 127:213–228
- Gasser TC, Görgülü G, Folkesson M, Swedenborg J (2008) Failure properties of intraluminal thrombus in abdominal aortic aneurysm under static and pulsating mechanical loads. J Vasc Surg 48(1):179–188
- Geest JPV, Sacks MS, Vorp DA (2006) A planar biaxial constitutive relation for the luminal layer of intra-luminal thrombus in abdominal aortic aneurysms. J Biomech 39(13):2347–2354
- Gersh KC, Nagaswami C, Weisel JW (2009) Fibrin network structure and clot mechanical properties are altered by incorporation of erythrocytes. Thromb Haemost 102(6):1169–75
- Holzapfel GA (2000) Nonlinear solid mechanics: a continuum approach for engineering. Wiley, Chichester
- Hughes TJR, Cottrell JA, Bazilevs Y (2005) Isogeometric analysis: CAD, finite elements, NURBS, exact geometry and mesh refinement. Comput Methods Appl Mech Eng 194:4135–4195

Janmey P.A, Amis E.J, Ferry J.D (1983) Rheology of fibrin clots. VI. Stress relaxation, creep, and differential dynamic modulus of fine clots in large shearing deformations. J Rheol 27(2):135–153

- Johnson S, Duffy S, Gunning G, Gilvarry M, McGarry JP, McHugh PE (2017) Review of mechanical testing and modelling of thrombus material for vascular implant and device design. Ann Biomed Eng 45(11):2494–2508
- Khodaee F, Vahidi B, Fatouraee N (2016) Analysis of mechanical parameters on the thromboembolism using a patient-specific computational model. Biomech Model Mechanobiol 15(5):1295–1305
- Kim OV, Liang X, Litvinov RI, Weisel JW, Alber MS, Purohit PK (2016) Foam-like compression behavior of fibrin networks. Biomech Model Mechanobiol 15(1):213–228
- Kim OV, Litvinov RI, Alber MS, Weisel JW (2017) Quantitative structural mechanobiology of platelet-driven blood clot contraction. Nature Commun 8:1–10
- Lam WA, Chaudhuri O, Crow A, Webster KD, Kita A, Huang J, Fletcher DA et al (2011) Mechanics and contraction dynamics of single platelets and implications for clot stiffening. Nat Mater 10(1):61–66
- Latorre M, Montáns FJ (2015) Anisotropic finite strain viscoelasticity based on the Sidoroff multiplicative decomposition and logarithmic strains. Comput Mech 56:503–531
- Lee YU, Lee A, Humphrey J, Rausch M (2015) Histological and biomechanical changes in a mouse model of venous thrombus remodeling. Biorheology 52:235–245
- Liu H, Holzapfel GA, Skallerud BH, Prot V (2019) Anisotropic finite strain viscoelasticity: constitutive modeling and finite element implementation. J Mech Phys Solids 124:172–188
- Liu W, Jawerth L, Sparks E, Falvo M, Hantgan R, Superfine R, Lord S, Guthold M (2006) Fibrin fibers have extraordinary extensibility and elasticity. Science 313(5787):634–634
- Malone F, McCarthy E, Delassus P, Fahy P, Kennedy J, Fagan A, Morris L (2018) The mechanical characterisation of bovine embolus analogues under various loading conditions. Cardiovasc Eng Technol 9(3):489–502
- Münster S, Jawerth LM, Leslie BA, Weitz JI, Fabry B, Weitz DA (2013) Strain history dependence of the nonlinear stress response of fibrin and collagen networks. Proc Natl Acad Sci 110(30):12197–12202
- Nedjar B (2016) On constitutive models of finite elasticity with possible zero apparent Poisson's ratio. Int J Solids Struct 91:72–77
- Ogden R (1973) Large deformation isotropic elasticity-on the correlation of theory and experiment for incompressible rubberlike solids. Rubber Chem Technol 46:398–416
- Ostwald R, Kuhl E, Menzel A (2019) On the implementation of finite deformation gradient-enhanced damage models. Comput Mech 64(3):847–877
- Piechocka IK, Bacabac RG, Potters M, MacKintosh FC, Koenderink GH (2010) Structural hierarchy governs fibrin gel mechanics. Biophys J 98(10):2281–2289
- Rausch MK, Humphrey JD (2016) A microstructurally inspired damage model for early venous thrombus. J Mech Behav Biomed Mater 55:12–20
- Rausch MK, Humphrey JD (2017) A computational model of the biochemomechanics of an evolving occlusive thrombus. J Elast 129:125–144
- Reeps C, Maier A, Pelisek J, Härtl F, Grabher-Meier V, Wall W, Essler M, Eckstein HH, Gee M (2013) Measuring and modeling patient-specific distributions of material properties in abdominal aortic aneurysm wall. Biomech Model Mechanobiol 12(4):717–733
- Reese S, Govindjee S (1998) A theory of finite viscoelasticity and numerical aspects. Int J Solids Struct 35:3455–3482
- Schulte R, Ostwald R, Menzel A (2020) Gradient-enhanced modelling of damage for rate-dependent material behaviour—a parameter identification framework. Materials 13:3156



- Sengupta D, Kahn AM, Kung E, Moghadam ME, Shirinsky O, Lyskina GA, Burns JC, Marsden AL (2014) Thrombotic risk stratification using computational modeling in patients with coronary artery aneurysms following Kawasaki disease. Biomech Model Mechanobiol 13(6):1261–1276
- Sugerman GP, Kakaletsis S, Thakkar P, Chokshi A, Parekh SH, Rausch MK (2021) A whole blood thrombus mimic. Constitutive behavior under simple shear. J Mech Behav Biomed Mater 115:104216
- Sugerman GP, Parekh SH, Rausch MK (2020b) Nonlinear, dissipative phenomena in whole blood clot mechanics. Soft Matter 16(43):9908–9916
- Tutwiler V, Singh J, Litvinov R.I, Bassani J.L, Purohit P.K, Weisel J.W (2020) Rupture of blood clots: mechanics and pathophysiology. Sci Adv 6(35):eabc0496
- van Dam EA, Dams SD, Peters GW, Rutten MC, Schurink GWH, Buth J, van de Vosse FN (2008) Non-linear viscoelastic behavior of abdominal aortic aneurysm thrombus. Biomech Model Mechanobiol 7(2):127
- van Kempen TH, Donders WP, van de Vosse FN, Peters GW (2016) A constitutive model for developing blood clots with various compositions and their nonlinear viscoelastic behavior. Biomech Model Mechanobiol 15:279–291
- van Oosten AS, Chen X, Chin L, Cruz K, Patteson AE, Pogoda K, Shenoy VB, Janmey PA (2019) Emergence of tissue-like mechanics from fibrous networks confined by close-packed cells. Nature 573:96–101

- Waffenschmidt T, Polindara C, Menzel A, Blanco S (2014) A gradient-enhanced large-deformation continuum damage model for fibre-reinforced materials. Comput Methods Appl Mech Eng 268:801–842
- Wang Y, Kumar S, Nisar A, Bonn M, Rausch MK, Parekh SH (2021) Probing fibrin's molecular response to shear and tensile deformation with coherent Raman microscopy. Acta Biomaterialia 121:383–392
- Weisel JW (2004) The mechanical properties of fibrin for basic scientists and clinicians. Biophys Chem 112(2–3):267–276
- Wendelboe AM, Raskob GE (2016) Global burden of thrombosis: epidemiologic aspects. Circ Res 118:1340–1347
- Zhang T, Lin S, Yuk H, Zhao X (2015) Predicting fracture energies and crack-tip fields of soft tough materials. Extreme Mech Lett 4:1–8
- Zitnay JL, Li Y, Qin Z, San BH, Depalle B, Reese SP, Buehler MJ, Yu SM, Weiss JA (2017) Molecular level detection and localization of mechanical damage in collagen enabled by collagen hybridizing peptides. Nat Commun 8(1):1–12

Publisher's Note Springer Nature remains neutral with regard to jurisdictional claims in published maps and institutional affiliations.

